IOP Publishing | International Atomic Energy Agency Nuclear Fusion

Nucl. Fusion **56** (2016) 056008 (16pp) doi:10.1088/0029-5515/56/5/056008

High frequency pacing of edge localized modes by injection of lithium granules in DIII-D H-mode discharges

A. Bortolon[1], R. Maingi[1], D.K. Mansfield[1], A. Nagy[1], A.L. Roquemore[1], L.R. Baylor[2], N. Commaux[2], G.L. Jackson[3], E.P. Gilson[1], R. Lunsford[1], P.B. Parks[3], C. Chrystal[4], B.A. Grierson[1], R. Groebner[3], S.R. Haskey[1], M.J. Makowski[5], C.J. Lasnier[5], R. Nazikian[1], T. Osborne[3], D. Shiraki[2] and M.A. Van Zeeland[3]

[1] Princeton Plasma Physics Labortory, Princeton, NJ 08543, USA
[2] Oak Ridge National Laboratory, Oak Ridge, TN 37831, USA
[3] General Atomics, PO Box 85608, San Diego, CA 92186, USA
[4] Oak Ridge Associated Universities, Oak Ridge, TN 37831, USA
[5] Lawrence Livermore National Laboratory, CA 94550, USA

E-mail: abortolon@pppl.gov

Received 6 January 2016, revised 22 February 2016
Accepted for publication 29 February 2016
Published 8 April 2016

Abstract

A newly installed Lithium Granule Injector (LGI) was used to pace edge localized modes (ELM) in DIII-D. ELM pacing efficiency was studied injecting lithium granules of nominal diameter 0.3–0.9 mm, speed of 50–120 m s^{-1} and average injection rates up to 100 Hz for 0.9 mm granules and up to 700 Hz for 0.3 mm granules. The efficiency of ELM triggering was found to depend strongly on size of the injected granules, with triggering efficiency close to 100% obtained with 0.9 mm diameter granules, lower with smaller sizes, and weakly depending on granule velocity. Robust ELM pacing was demonstrated in ITER-like plasmas for the entire shot length, at ELM frequencies 3–5 times larger than the 'natural' ELM frequency observed in reference discharges. Within the range of ELM frequencies obtained, the peak ELM heat flux at the outer strike point was reduced with increasing pacing frequency. The peak heat flux reduction at the inner strike point appears to saturate at high pacing frequency. Lithium was found in the plasma core, with a concurrent reduction of metallic impurities and carbon. Overall, high frequency ELM pacing using the lithium granule injection appears to be compatible with both H-mode energy confinement and attractive H-mode pedestal characteristics, but further assessment is needed to determine whether the projected heat flux reduction required for ITER can be met.

Keywords: tokamak, ELM, pacing, pellet, mitigation, heat load, control

(Some figures may appear in colour only in the online journal)

1. Introduction

Naturally-occurring, periodic relaxations of the plasma edge called Edge Localized Modes (ELM), are characteristic of H-mode confinement in diverted tokamak plasmas, and, if unmitigated, are likely to cause unacceptable damage to wall components in next-step tokamak fusion devices [1]. Present day projections indicate that safe operation in ITER [2] would require a 20–50 fold reduction in the peak heat flux deposited on the divertor tiles during a spontaneous ELM event [3]. This motivates the development of reliable techniques to suppress ELMs or mitigate their detrimental effects [4]. Experimental demonstration of mitigation has been obtained in several tokamak devices, by actively inducing ELMs at frequencies

much larger than the existing natural ELM frequency, thus effectively reducing the amount of energy per ELM lost by the plasma and conveyed onto divertor tiles [5–7]. While reliable and effective ELM pacing, with corresponding ELM peak heat flux reduction, has been achieved by injection of deuterium pellets into carbon-walled tokamaks, the reduction of peak heat flux with high frequency ELM pacing in metal-walled tokamaks has been marginal [8, 9]. In addition, there is concern about the amount of deuterium throughput required to maintain robust, high-frequency ELM pacing in ITER, where the total fuel throughput in the vessel will be limited by the capacity of pumping and tritium processing systems [10]. In that regard, the use of non-fuel pellets, e.g. low Z non-recycling elements such as lithium (Li) or beryllium (Be), would alleviate the load on the gas post-processing systems, by decoupling ELM pacing from plasma fueling.

A simple prototype device capable of injecting small spherical lithium granules at velocities up to $\sim$100 m s^{-1} was shown to trigger ELMs in the EAST tokamak [11]. Building on that experience, an upgraded version of the lithium granule injector (LGI) was recently installed on DIII-D, to study the dependence of pacing efficiency on granule size and velocity, and more generally characterize LGI-induced ELMs.

Generally, the DIII-D experiments reported in this work demonstrate that periodic ELM triggering at high frequencies can be achieved by lithium granule injection, while preserving the integrity of the discharge. Notably, ELM pacing for a full discharge pulse length was obtained, while maintaining good normalized energy confinement as compared to reference discharges with naturally occurring ELMs.

The remainder of the article is organized as follows: introduction of the experimental apparatus and techniques (section 2), discussion of the results in terms of triggering efficiency (section 3.1), presentation of discharge performance (section 3.2), and reduction of divertor heat loads (section 3.3). The last section summarizes the results and discusses the outlook for this new technique.

2. LGI implementation and operation

The LGI was developed as a tool to deliver controlled amounts of lithium inside the last closed flux surface. To this end, the LGI injects submillimiter-scale spherical lithium pellets, i.e. granules, at velocities on the order of 100 m s^{-1}.

A detailed description of the LGI apparatus and operation can be found in [11]. In its essence, the system combines a two-paddle rotating 'impeller', with a vibrational granule dropper (figure 1(*a*)). In the dropper, granules are loaded on a piezo-electric disk with a central aperture. The piezo-electric disk is energized with an oscillating voltage, tuned to excite a resonant vibrational mode of the disk. In response to the mechanical oscillation, granules fall through the aperture, into a vertical guiding tube that leads to a rotating impeller blade. Upon impact with the impeller blade, granules are propelled horizontally towards the plasma edge.

As implemented on DIII-D, the LGI offers a wide range of choices for granule size, injection rate and injection velocity. The dropper is equipped with four separate granule reservoirs that can be used to inject different kinds or sizes of granules. For these experiments, the reservoirs were loaded with lithium granules of nominal diameter 0.3, 0.4, 0.7 and 0.9 mm. The actual granule diameter in each set varies within $\pm$0.1 mm from the nominal diameter. Manual selection of the injected granule size was accomplished between plasma discharges, by changing the reservoir employed by the turn of a vacuum rotary feed-through.

The granule injection rate is approximately proportional to the voltage applied to the piezo-electric disc, up to a saturated value, that depends on the granule diameter. Average injection rates can be obtained up to 100, 200, 500 and 1000 Hz for 0.9, 0.7, 0.4 and 0.3 mm diameter respectively.

The granule injection velocity is directly proportional to the LGI impeller rotation frequency. At the nominal maximum rotation frequency of 250 Hz, the impeller blade velocity at the location of the granule impact is $v_{\rm imp} \approx 85$ m s^{-1}. In a fully elastic impact, a projectile would acquire a velocity of $v_{\rm g} = 2v_{\rm imp}$. However, in the case of lithium granules, the actual relation inferred from measurement is $v_{\rm g} \approx 1.3 v_{\rm imp}$, indicative of a deeply inelastic impact, quantifiable with an average coefficient of restitution $C_{\rm R} \approx 0.3$ (for a definition of the coefficient of restitution see for example [12] and references therein).

For the experiments reported here, the LGI was installed on DIII-D with a nominally horizontal injection trajectory directed radially at the outboard mid-plane (figure 2). The injection location was at toroidal machine angle of 285°. For reference, the location of the vertical infrared thermography view of the divertor was at 60°, and the location of the outboard deuterium pellet injection was at 135°.

In the present design, the LGI does not allow for precise timing of individual injections. In fact, due to the asynchronous operation of the dropper and impeller, the injection rate can only be controlled in a time-average sense. Throughout this paper, the term 'ELM pacing' will be used to describe a situation in which nearly 100% of observed ELMs are triggered by granule injections, disregarding the periodicity of the pacing.

In order to monitor the system operation and document its performance, the LGI was equipped with a set of diagnostics, schematically depicted in figure 1(*b*). A fast camera (Phantom 7.3, by Vision Research [13]), installed on the side of the impeller chamber, was used to record the impeller-granule impact region. Acquisitions of 100×300 pixel images at 20 kHz frame rate accurately resolved the moving granules falling out of the guide tube, and permitted the determination of the impact times with 50 μs precision. Two small halogen lamps, each equipped with a focusing lens, provided adequate illumination of the impeller impact zone, figure 3(*a*).

Image processing tools were applied off-line to the side-view camera data so as to recover the evolution of several operational quantities: (1) granule diameters, (2) number of granules per impact, (3) time of injection, (4) impeller rotation frequency $f_{\rm imp}$, (5) granule drop rate $f_{\rm drop}$, and (6) the injection frequency $f_{\rm inj}$. Figures 3(*b*) and (*c*) illustrates two typical outputs of the analysis for an experiment using granules of nominal diameter 0.4 mm and with $f_{\rm imp} = 250$ Hz: the distribution of the granule diameters and the spectrum of injection

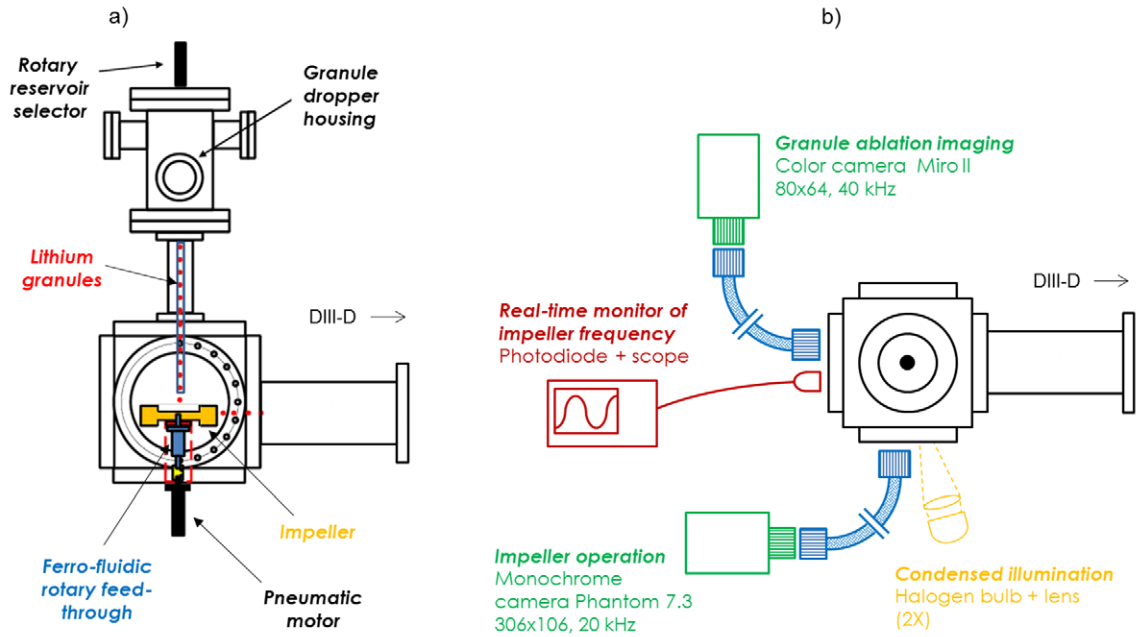

Figure 1. Schematic representation of the lithium granule injector, illustrating the working principle (*a*) and the diagnostic instruments available (*b*).

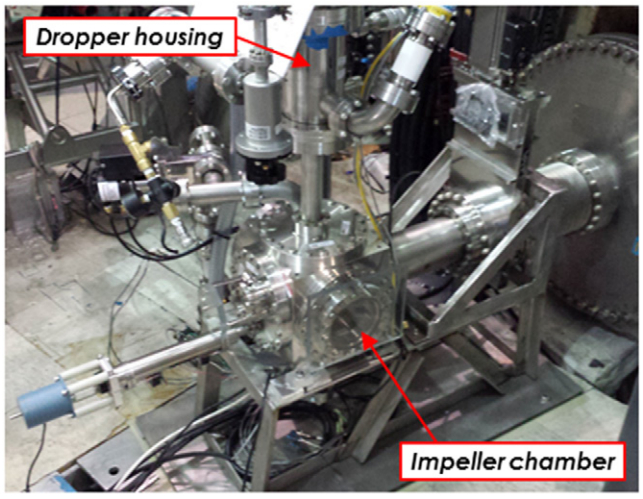

Figure 2. The LGI system as implemented on a equatorial port of DIII-D.

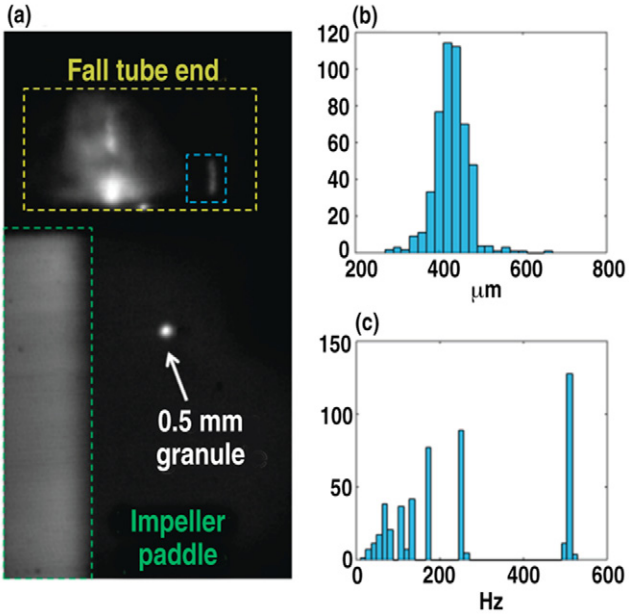

Figure 3. (*a*) Image captured by the fast camera monitoring the operation of the impeller, before a 0.5 mm diameter granule is hit and launched towards the plasma. The injection direction is from left to right in this image. Highlighted in colored boxes are the thin side impeller blade (green) moving from left to right and aligned with the view at this time, and the end of the guide tube (yellow). The blue box encircles a region where light from granule ablation in the plasma is reflected, and used to track the ablation events. (*b*) Distribution of granule sizes determined from the fast camera frames for a single discharge with nominal diameter 0.4 mm. (*c*) A spectrum of the injection frequency can be constructed from the series of the inter-injection periods. In this case the spectrum shows a dominant component at 500 Hz, associated with the 250 Hz rotation frequency of the 2-paddle impeller.

frequencies. The latter corresponds to the distribution of the inverse of inter-injection periods and can be used to evaluate the variation of the period of injection: for the case in figures 3(*b*) and (*c*), the peak at $250 \times 2 = 500$ Hz corresponds to the maximum injection frequency, achieved when the drop rate $f_{\mathrm{drop}} \gtrsim 500$ Hz, while peaks at 250, 166, 125 Hz arise from transient phases with drop rate <500 Hz.

The side camera field-of-view includes internal structural elements of the LGI assembly that directly reflect light emitted from the plasma, projected outwards through the flight tube. By tracking in time these reflections, a time history of granule ablation events can be constructed. This 'ablation monitor'

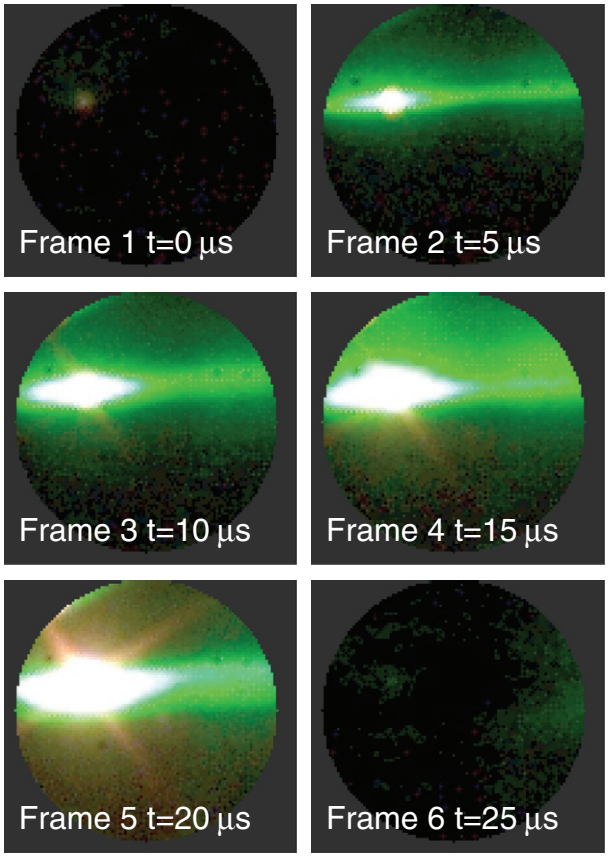

Figure 4. Sequence of fast camera imaging capturing the ablation of a 0.4 mm diameter lithium granule, injected in the plasma at 100 m s^{-1}. The end of the injection tube limits the view to a circular area of ≈30 cm diameter, at the plasma edge. The 10° tilt of the elongated ablation cloud reflects the pitch of magnetic field in the plasma edge.

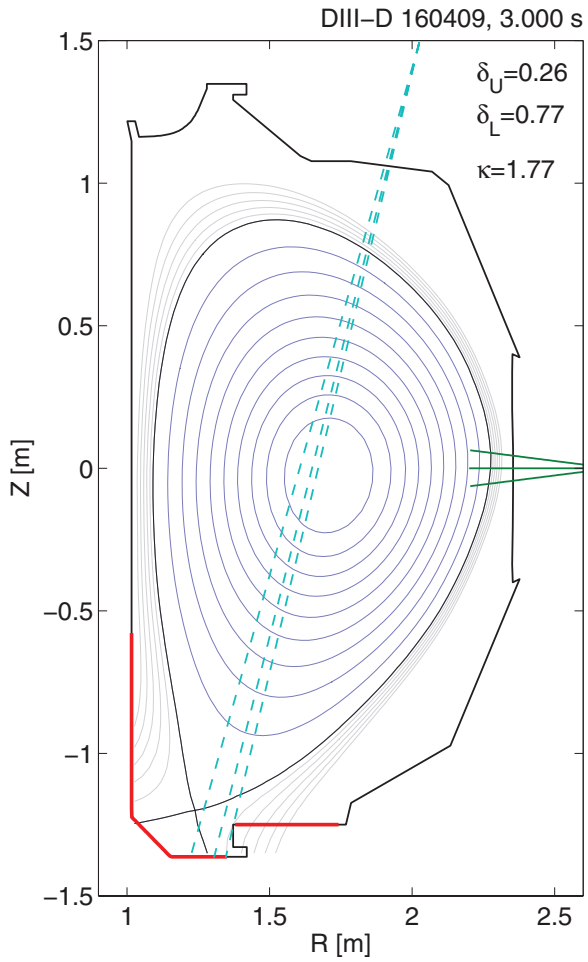

Figure 5. Magnetic configuration of the reference plasma discharge. The solid angle covering the injection of the lithium granules is depicted at the LFS equatorial plane. The dashed lines corresponds to the filter-scope chords for the D_α measurement used as ELM monitor. The region of the divertor tiles highlighted in red corresponds to the area observed by the infrared thermography camera (IRTV).

was used to discriminate between injections that reached the plasma from those that did not transit successfully through the flight tube. This procedure allowed the measurement of an effective injection efficiency, defined as the number of granules ablated per number of granules dropped. In these experiments the injection efficiency was typically ∼85% or larger. In addition, by cross-correlating the time histories of granule impacts and ablation events, the granule times-of-flight were measured, and led directly to the granule injection velocities.

A real-time monitor of the impeller rotation frequency was obtained by frequency analysis of a photo-diode signal, which tracked the periodic fluctuation of the background light in the main chamber of the LGI, caused by the rotation of the impeller (figure 1(*b*)).

Finally, a fast color camera (Miro II, by Vision Research [13]) was used to observe the plasma edge from a window located on the back of the LGI body, thus providing a radial view of the ablation region through the LGI injection tube. The available field-of-view was defined by the end of the flight tube, and mapped to an area of ≈30 cm diameter at the plasma boundary. Acquisitions of color images at frame rates up to 40 kHz were able to capture the dynamics of the granule ablation/penetration, characterized by the expansion of a field-aligned cloud of ablated material. An example of ablation of a Li granule is shown in the sequence of camera frames in figure 4, where the color images are dominated by green line emission at 548 nm, from singly ionized Li II. The number of frames associated with each ablation event provides an estimate of the granule ablation time, i.e. the time required for the injected granule to ablate and ionize completely, as it propagates inward. Under the assumption of constant propagation velocity, a penetration depth can be inferred, which, as discussed in section 3.1, was found to be 2–8 cm, depending on granule size, injection velocity and pedestal characteristics.

3. Experimental results

For the experiments reported in this work, reference discharges were developed which were similar to discharges employed in previous experiments on ELM pacing with deuterium pellets in DIII-D [14], i.e. a deuterium plasma, confined in a lower single null configuration with an ITER-like shape (figure 5). Typical discharge parameters were as follows: $B_t = 2.0$ T, $I_p = 1.2$ MA, $q_{95} \approx 4.6$, $\beta_N \approx 1.5$. These reference discharges

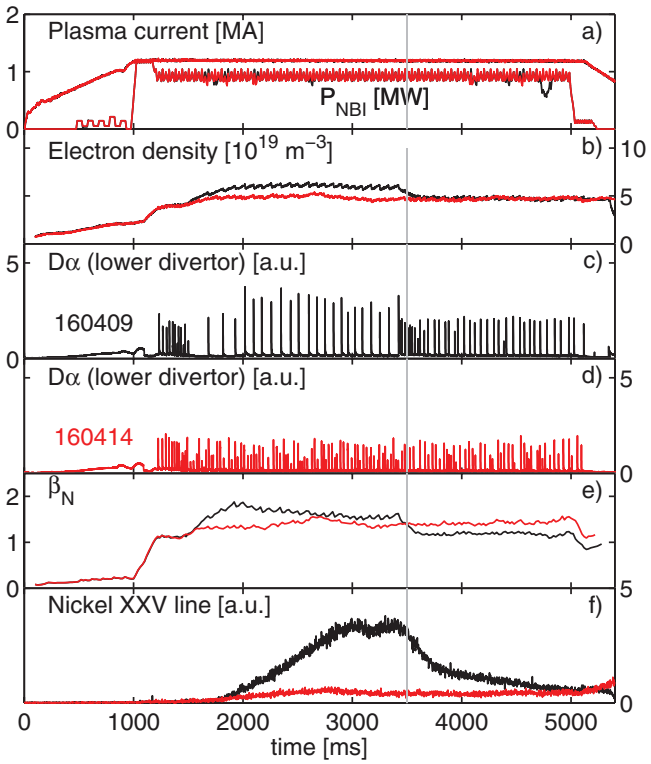

Figure 6. Evolution of selected plasmas parameters, for a reference discharge with spontaneous ELM activity (160409, black) and a discharge with LGI ELM pacing (160414, red). In the reference discharge the onset of an $n = 2$ mode, deteriorates the confinement for $t \geqslant 3.5$ s.

were characterized by robust periodic type-I ELM activity. The ion $\vec{B} \times \nabla B$ drift was directed downwards, and thus was favorable for H-mode access with low L-H power threshold. Because the neutral beam heating $P_{\mathrm{NBI}} = 4$ MW was only slightly above the L-H power threshold, the natural ELM frequency was a relatively low 12 Hz. It should be noted that that only NB injection in the direction of plasma current was used, which resulted in a relatively high torque of 2.9 N m, and, consequently, carbon toroidal rotation of $\approx$30 km s^{-1} in the pedestal region. In these experiments, the plasma facing components consisted entirely of carbon tiles.

Figure 6 illustrates the evolution of a selection of discharge parameters for the reference discharge (160409) and a discharge with ELM pacing by lithium granule injection (160414). The appearance of MHD modes is common in this operating scenario, and is likely associated with the radiative cooling of the core from the accumulation of metal impurities. This phenomenology can be seen to occur in the reference discharge, after $t = 3.5$ s, when the confinement deteriorates and ELM frequency increases, due to the onset of an $n = 2$ MHD mode.

For the ELM-pacing discharge shown, 0.4 mm diameter granules were injected from $t = 1.5$–5.0 s, with an average velocity of $v_g \approx 109$ m s^{-1} and at an average injection rate of 140 Hz. The ELM activity is indicated by the evolution of D_α emission measured by a filter-scope aimed at the outer strike point region (figure 5). The D_α trace in figure 6(d) shows a substantial increase in the frequency of spikes associated with ELMs, as compared to the reference discharge in figure 6(c). Indeed, correlation with pellet injection monitors indicates that ELM pacing was achieved for the entire discharge, with 98% of the ELMs destabilized in response to a granule injection. However, only $\approx$30% of the injected granules triggered an ELM. As a result, LGI injection resulted in a $\approx$3-fold increase of the average ELM frequency, from 12 to 38 Hz.

In other discharges, where LGI was applied for shorter durations of $\approx$0.5–1.0 s, higher average ELM frequencies were attained, up to a factor of 5 over the natural ELM frequency.

The high-frequency pacing resulted in lower electron density, as exemplified in figure 6(b) where the line integrated density during the flat top $n_e = 5 \times 10^{19}$ m^{-2}, was reduced by 10% compared with the reference discharge. Reduction of electron density by 5–10% was generally observed, even in cases of high-frequency injection of largest granules (0.7–0.9 mm). This indicates that the increased particle exhaust associated with the high frequency ELMs exceeded the additional source of electrons from lithium ionization. available granules.

Contrary to what was observed in the reference discharge, during LGI ELM pacing the accumulation of metal impurities did not take place. In these quasi-stationary discharges, the brightness of the Ni XXV line at 117 nm measured by the SPRED survey spectrometer, quantifies plasma core contamination by nickel. As shown in figure 6(f), in the LGI case the Ni XXV brightness remains constant throughout the discharge, 'clamped' at levels seen prior to Li granule injection. As a result of the lower metal impurity accumulation and lower β_N, LGI-paced discharges were also less prone to develop core MHD instabilities, as exemplified by discharge 160414, which remained virtually MHD free for the entire discharge flat-top.

In general, the DIII-D plasmas with LGI injection were found to be extremely resilient to high frequency Li injection, tolerating sustained mass injection rates up to $\approx$30 mg s^{-1}, which were obtained with 100 Hz injection of 0.9 mm granules, without incurring major instabilities or radiative collapse. However, back transitions to L-mode were observed when injecting 0.3 mm diameter granules at injection rates over 1 kHz, corresponding to mass rates of the order of 10 mg s^{-1}. In this case, the energy required to ionize the lithium amounted to 30 kW, i.e. $\approx$1% of the NBI injected power, suggesting that the back transition is associated with the changes of the plasma boundary characteristics, possibly in a local fashion, more than with a reduction of the effective input power.

3.1. ELM triggering efficiency and ELM pacing

ELM triggering and pacing was studied by varying the lithium granule injection parameters, e.g. size, velocity and rate, in an H-mode reference discharge. In general, the experiments demonstrated the ELM triggering for all granule sizes tested. This is exemplified in figure 7, which compares the divertor D_α trace against the ablation monitor trace. The latter was constructed from the locally-emitted ablation light as described in

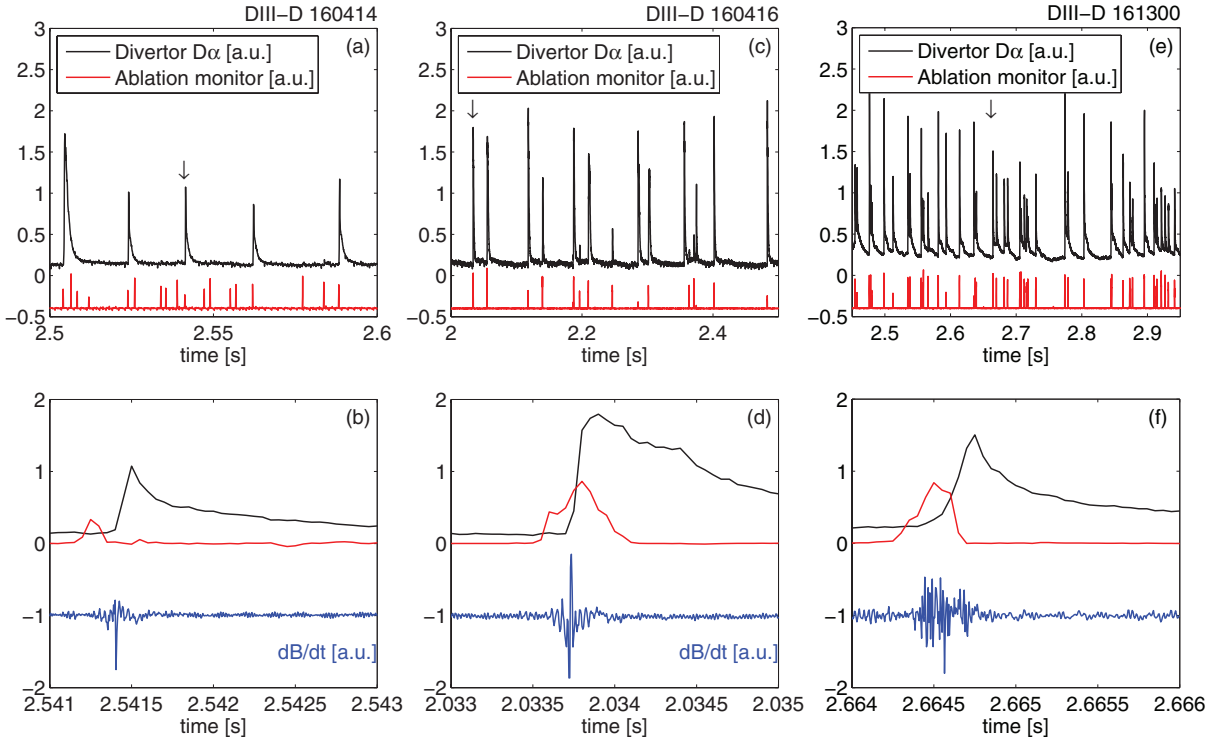

Figure 7. Examples of ELM pacing achieved with three combinations of granule diameter and average injection frequency: 0.4 mm at 140 Hz ((*a*), (*b*)), 0.7 mm at 60 Hz ((*c*), (*d*)) and 0.9 mm at 100 Hz ((*e*), (*f*)). ELMs marked by a vertical arrow in the top panels are shown in detail in the bottom panels. In the three experiments, nearly all ELMs were triggered by a granule ablation event. When using 0.7 or 0.9 mm granules, nearly all ablation events triggered and ELM.

section 2. The figure includes measurements from three discharges in which pacing was tested with granule diameters 0.4, 0.7 and 0.9 mm, respectively. The bottom panels show an expanded view of single ELM events, including the signal from an in-vessel magnetic Mirnov probe, located on the equatorial plane at toroidal machine angle 132°.

All the ELMs included in figure 7 took place in response to an ablation event. A spike in the magnetic signal, interpreted as the signature of an ELM crash, is typically observed 100–300 μs following the initiation of an ablation event. This delay approximately corresponds to the time required for a granule traveling at $v_g = 100$ m s^{-1}, to reach the top of the pedestal in these discharges. The D_α signal from the outer divertor increases within 0.5–1 ms after the onset of ablation light. This time is somewhat longer than the ≈0.5 ms ELM transit time, i.e. the time required for a mid-plane relaxation to reach the divertor, by parallel propagation, estimated for this configuration.

The probability that an ELM would be triggered by an injected granule was seen to depend strongly on the granule size. In particular the injection of either 0.7 mm or 0.9 mm diameter granules almost always resulted in an ELM, while in the case of 0.4 mm granules, only a fraction of the ablation events triggered an ELM. In fact, approximately 70% of the 0.4 mm granules were absorbed by the plasma with almost undetectable effects on D_α emission or heat flux deposition. These observations are summarized in figure 8(*a*), where the probability of triggering an ELM is shown for different sizes and injection velocities. In this figure, each data point is taken from a time window of an ELM-paced discharge, drawing on a set 15 different discharges. Data points are marked in black for injection velocity $v_g = 95$–120 m s^{-1}, and red for $v_g = 50$–65 m s^{-1}. It can be seen that larger granules (0.7 and 0.9 mm) approach 100% efficiency in triggering ELMs, in the plasma parameter range explored. On the other hand, smaller granules have low efficiency 15–30%. Also, the triggering efficiency tends to degrade with reduced velocity.

Observations of ELM-pacing frequencies that are much smaller than the actual granule injection frequencies, as for instance in the case of figure 7(*a*), suggest the existence of an upper limit for the ELM-pacing frequency, attainable with specific granule size, or perturbation amplitude. On the other hand, because control of the LGI injection frequency is imperfect, rapid sequences of multiple injections can be seen in the data. This is exemplified in figure 7(*e*), when, at $t = 2.92$ s a group of 5 ELMs were triggered with an inter-ELM period of ≈5 ms, which translated into an 'instantaneous' ELM frequency of ≈200 Hz. These rapid sequences, in the case of injection of larger pellets, demonstrate that, at least transiently, the maximum achievable frequency can greatly exceed the average injection rate delivered by the LGI.

Non-linear modeling of pellet-induced ELMs has correlated the efficiency of ELM triggering with the ability of the pellet to reach the pedestal top or beyond [15]. This prediction can be addressed experimentally by determining the granule penetration depth from the light emitted during the ablation. Figure 4 shows a sequence of images captured by a fast-framed color camera, observing the plasma radially, along the granule flight tube. Each ablation begins with a ≈1 cm diameter yellow cloud (ascribed to a combination of neutral Li lines, from

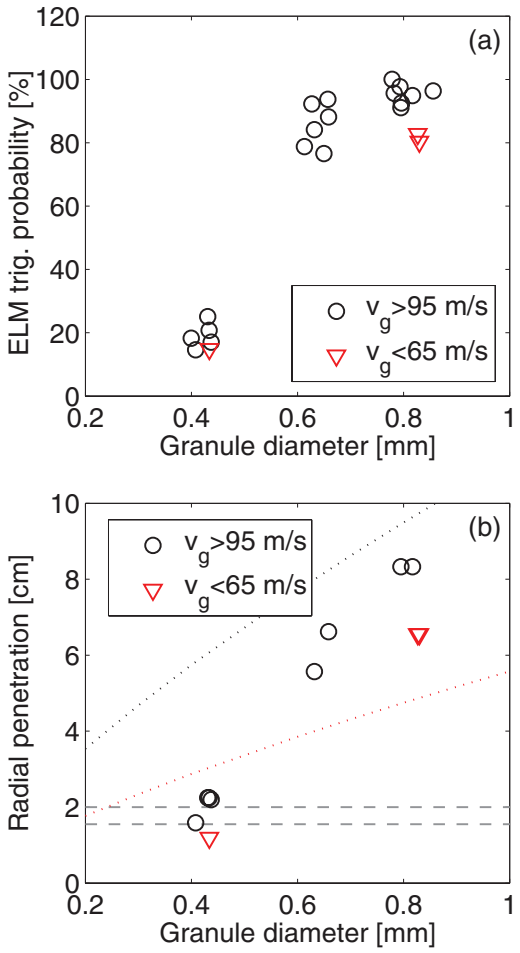

Figure 8. (*a*) Probability of triggering an ELM by lithium granule injection as a function of granule diameter, obtained in a number of different LGI discharges with LGI pacing. The probability corresponds to the ratio between the number of ELMs and the number of ablation events observed during selected time windows. (*b*) Averaged granule penetration depth as a function of the injected granule diameter, obtained from the ablation durations, under the assumption of constant granule speed. The dashed lines indicate the radial range where the pressure pedestal top is found in the reference discharge. The dotted curves represent the expected penetration depth according to the prediction of a lithium granule ablation model, for two values of granule velocity 50 and 100 m s^{-1}.

different spectral regions, including Li I 460, 610 and 670 nm) which develops into a field aligned green emission (singly ionized Li II line at 548 nm). The frame count of images showing granule ablation provided an estimate of the ablation time, which, under the assumption of constant penetration velocity, translated into penetration depth, i.e. the distance the pellet traveled inside the separatrix before full evaporation.

The penetration depths estimated for different cases are shown in figure 8(*b*). It is clear that the larger granules penetrated beyond the pedestal top, while the smaller granules were ablated in the pedestal. This result is qualitatively consistent with pellet ablation theory, predicting the ablation time to depend primarily on the pellet mass, and to a lesser extent on velocity [16, 17]. Figure 8(*b*), also includes the penetration depths predicted by the NGS ablation model [18], recently extended to treat pellets composed of refractory materials down to full ablation. The predictions utilize experimental kinetic profiles for the background plasma and assume constant granule velocity during the ablation. The model agrees with the experimental data within 10–30%, for larger granule sizes, with a tendency to overestimate the penetration of faster granules. Given the uncertainties associated with the single granule characteristics (for instance actual mass, shape) this agreement might be considered reasonable. However, in the case of 0.4 mm granules, a significant overestimation of the ablation time is found, which is presently under investigation.

The amplitude of LGI-triggered ELMs was found to vary significantly, as illustrated in figure 9(*a*), showing the distribution of ELM magnitude, quantified by the drop of plasma stored energy ΔW_{MHD} following each ELM event, in three different plasma discharges. The plasma stored energy evolution was determined through time dependent equilibrium reconstructions, performed with the EFIT [19] code, at 1 ms intervals, accounting for the measured kinetic pressure profiles, of electron, ions and beam ions. The time averaged stored energy amounted to $W_{\mathrm{MHD}} = 710$ kJ in the reference discharge, and was about 15% lower when pacing with 0.4 and 0.7 mm granules, $W_{\mathrm{MHD}} = 580$ kJ and 610 kJ respectively. While in the natural ELM case ΔW_{MHD} peaks at 55 kJ ($\Delta W_{\mathrm{MHD}}/W_{\mathrm{MHD}} \approx 8\%$), in the LGI paced scenarios the distribution is much broader, with $\Delta W_{\mathrm{MHD}} = 5$–40 kJ ($\Delta W_{\mathrm{MHD}}/W_{\mathrm{MHD}} \approx 1$–7%). A broader distribution is also found in the thermography measurements of the divertor heat loads, represented in figure 9(*b*), in terms of peak heat flux at the inner strike point (ISP). To a large extent, this variability can be ascribed to the non-periodic nature of the LGI injections, resulting in ELMs being triggered in different phases of the inter-ELM period. Indeed, anecdotal evidence indicates that often larger ELMs are triggered after long inter-ELM periods, while ELMs triggered immediately after a large ELM are smaller. However, as discussed in section 3.3, a clear correlation between the inter-ELM period and ELM amplitude could not be established, indicating that other elements are playing a role, for instance the variations in granule mass, velocity or pedestal characteristics, or nonlinear dynamics intrinsic to the ELM triggering process.

Furthermore, in ELM pacing experiments using 0.7 and 0.9 mm diameter granules, ELM events were observed, which were characterized by a small, distinct D_α signature, but were not correlated with a clearly detectable drop in pedestal density or fast signatures on magnetic probe signals. Figure 10 shows two sequential ELMs, observed in the same discharge in response to injection of 0.9 mm granules at 105 m s^{-1}. Both events begin with a slow increase of D_α emission, with similar characteristic timescales. However, a sudden increase in D_α emission occurs for the second ELM, which correlates with a spike in the magnetic signal, not detected in the first event. These observations suggest an interpretation of the granule triggered ELM as a two-step process, characterized by two different time scales: an initial perturbation of the axisymmetric equilibrium induced by the expansion of the granule ablation cloud, which itself can result in enhanced losses at the boundary, possibly followed by the sudden onset of an MHD instability, when the proper conditions are met. In this interpretation, during events like the first one in figure 10,

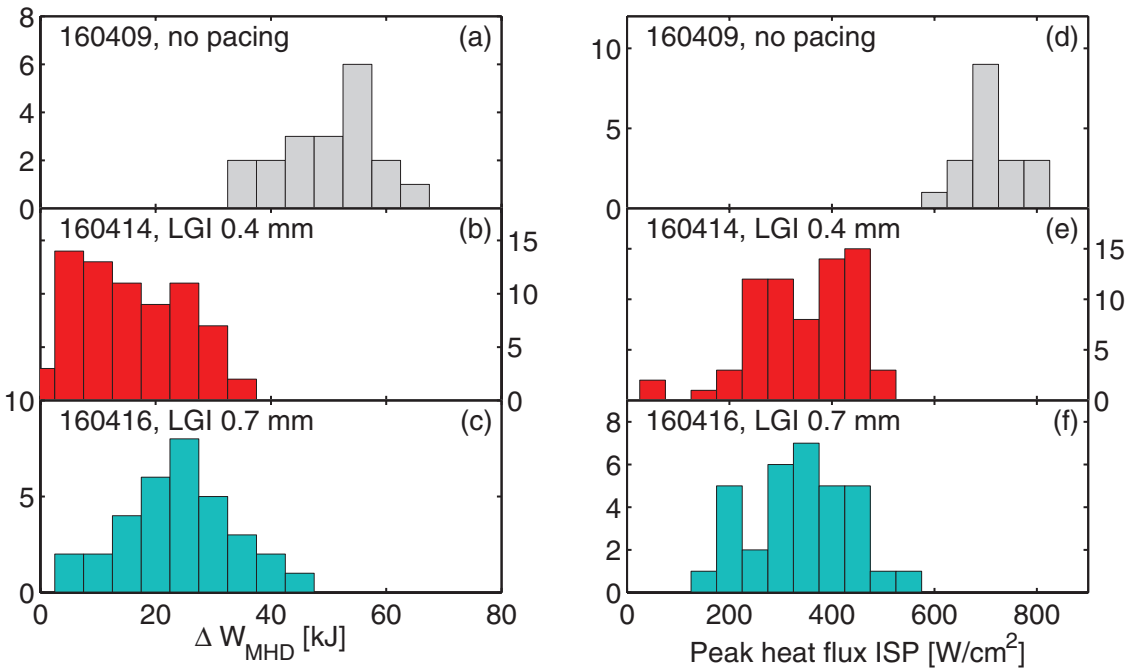

Figure 9. Distribution of ELM amplitudes, expressed in terms of drop in stored energy ΔW_{ELM} (left) and ELM peak heat flux q_{p} at the inner strike point (right), in three DIII-D discharges with different ELM pacing schemes.

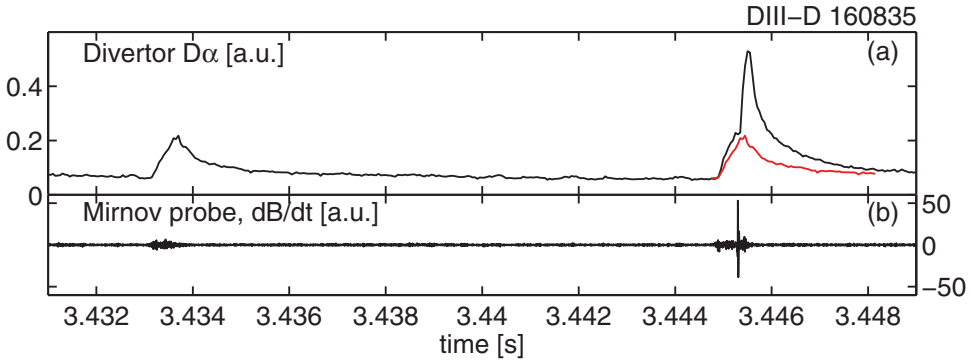

Figure 10. (*a*) D_α emission at the OSP resulting from two subsequent injections of 0.9 mm diameter Li granules. The D_α signature of the first event is superposed to the second event in red, to facilitate the comparison. The first event does not show the spike in the magnetic signal typically associated with a ELM.

the pellet induced perturbation was insufficient for bringing the pedestal to instability, a phenomenology reminiscent of the sub-threshold edge perturbations (STEP), induced on NSTX by means of externally applied 3D fields [20]. For the scenarios presented in this work the incidence of this type of event was minimal, but became more significant in discharges performed at low torque, whose study is left for future work.

Thus, the results of the pacing experiments support a link between the penetration depth and the ability to trigger ELMs at a given frequency. More insight into the problem requires a self-consistent treatment of the MHD stability, as performed for instance in [15].

3.2. Effect on plasma performance

While lithium granule injection increased the average ELM frequency by factors of 3–5×, the paced discharges departed from the reference scenario in several other aspects, as we report in this section with focus on plasma performance.

The lower values of β_N in the LGI discharge (figure 6), are reflected in the energy confinement time, which is reduced by ≈10% (figure 11(*a*)). This might in part be associated with the decrease in confinement time associated with the lower working density, expressed for example in the H-mode confinement factor $H_{98,y2}$ [21] which incorporates a density dependence of $H_{98,y2} \sim n_{\mathrm{e}}^{0.44}$. In fact, the confinement factor $H_{98,y2}$ is not observed to decrease (figure 11(*b*)). Figure 11 extends the comparison of plasma discharges 160414 and 160409, with and without LGI ELM pacing, respectively. In the ELM paced discharge (160414), a constant value of $H_{98} \approx 1.2$ is reached at $t = 1.5$ s and maintained for the rest of the current flat-top, matching the value measured in the reference discharge (160409) within $t = 2.5$–3.5 s, before the onset of the $n = 2$ MHD mode. Good confinement is also indicated

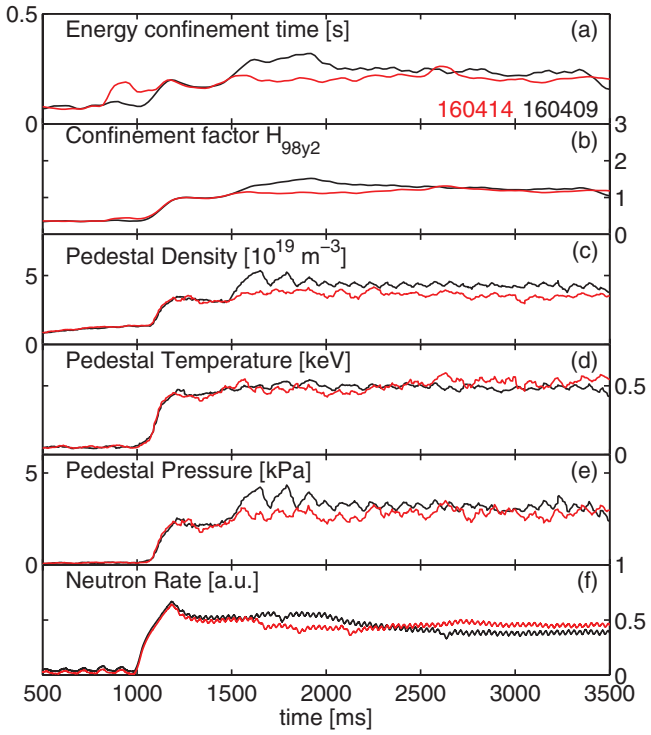

Figure 11. Evolution of selected parameters representative of the discharge performance and pedestal characteristics, for discharges 160414 (LGI) and 160409 (reference), also shown in figure 6.

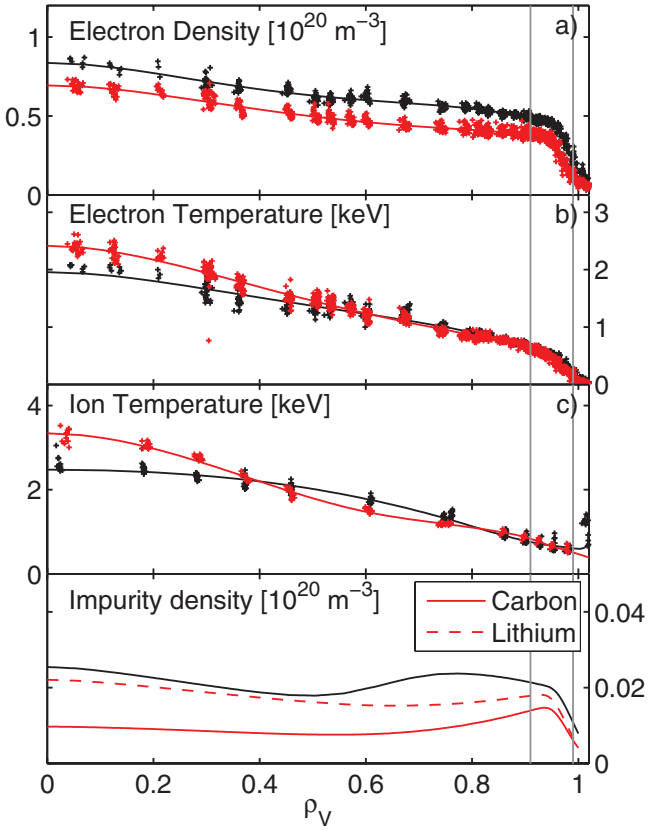

Figure 12. Comparison of background kinetic profiles between reference (black) and LGI (red) discharges. Dots represent data points measured within the last 10% of the inter-ELM period. Profiles are shown as a function of normalized plasma volume. Curves are the result of cubic spline fits to the data.

by the measured 10% increase of neutron production rate, visible in figure 11(*e*).

Panels (*b*)–(*d*) in the same figure show the evolution of electron density, temperature and pressure measured at the pedestal top, by Thomson scattering. The ≈10% decrease in pedestal electron density is partially compensated by a simultaneous increase of electron temperature T_e in the same region, thus resulting in an electron kinetic pressure reduced by 5%.

Inspection of the kinetic profiles, shown in figure 12 as a function of the normalized volume radial coordinate $\rho_V = \sqrt{V/V_a}$, reveals that while the entire radial profile of n_e decreases rigidly, following a reduction of the pedestal height, both electron and ion temperature profiles T_e and T_i become more peaked in the core. It should be noted that the profiles shown are averaged over a time window $t = 2.0$–3.5 s, selecting profiles measured during the last 5% of the inter-ELM period. As a result higher on-axis temperatures are observed, by 12% for T_e and 25% for T_i. This difference in temperature profile gradient and, consequently, on-axis value, might indicate a change in energy transport associated with the presence of lithium in the plasma core. However, it might also be ascribed to the measured 15% reduction of radiative losses, from 1.3 to 1.1 MW, as a result of smaller metal impurity concentration.

Indeed, during intense LGI operation, lithium was observed deep in the plasma core, while, at the same time, a substantially reduced concentration of the intrinsic metallic impurities was found. This is exemplified in figure 13, which, for three LGI discharges with different injection characteristics, shows the evolution of the intensity of the Li III line at 11.4 nm and the Ni XXV line at 11.7 nm. Both intensities were measured by the survey spectrometer SPRED, along a chord crossing the plasma core. A strong modulation of the Li III signal correlating with the NB injection waveforms, indicates that the measured emission largely consists of active charge-exchange from the NB, and, as such, represents a measurement of the Li III density at the $R = 1.7$ m, where the SPRED chord intersected the NB.

Figure 13(*a*) shows the evolution of the granule injection frequency, computed from the number of granule ablation events detected in a moving time interval of 200 ms. Clearly, the lithium granule injection results in an increase of lithium radiation from the core. Conversely, as LGI operation terminates, lithium concentration decreases towards zero, with a timescale of the order of ≈0.5–1 s.

Due to the lack of cross-section data for the Li III line, a local Li density could not be computed from the SPRED data. An estimate of the Li density profile can be made, however, by combining the carbon density profile and the visible bremsstrahlung measured by the DIII-D multi-chord charge-exhange recombination diagnostic (see appendix). The profile of n_{Li} determined in this way, is shown in figure 12, together with the carbon density profile n_C, indicating that Li fills the plasma core, with a roughly flat profile throughout the plasma minor radius and with values that are similar to the carbon density in the reference discharge. Interestingly, the carbon

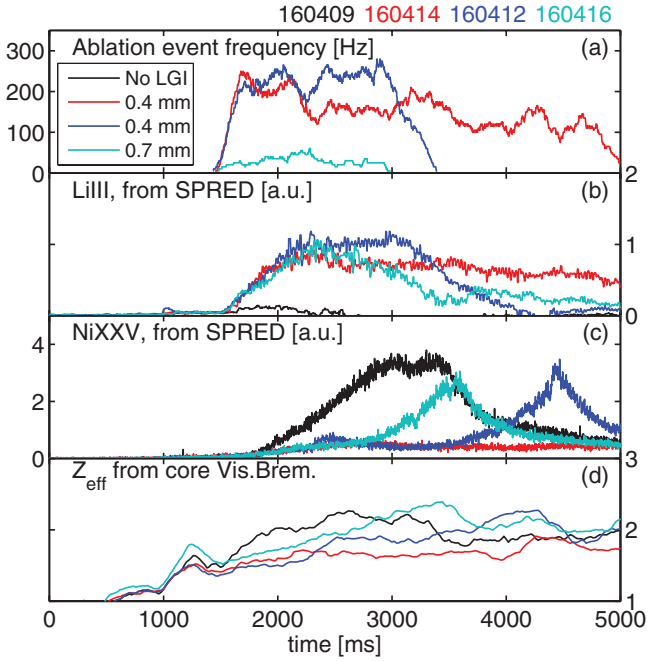

Figure 13. (*a*) Evolution of the lithium granule injection rate during four discharges with different LGI pacing schemes. The degree of accumulation of lithium and metal impurities can be inferred from the intensity of spectral lines Li III (*b*), and Ni XXV (*c*) measured by the SPRED diagnostic. The lower contamination from high charge impurities during ELM pacing combined with the reduced carbon density results in a lower line averaged $Z_{\rm eff}$, as inferred from chordal measurements of visible bremsstrahlung emission.

density in the LGI paced discharge is strongly reduced. These results are in qualitative agreement with previous observations in DIII-D discharges with lithium aerosol injection [22], and contrast with the very low level of lithium consistently measured in NSTX lithiated H-mode plasmas [23].

LGI operation was observed to prevent or delay the accumulation of metal impurities: figure 13 illustrates how during LGI phases, the emission from Ni XXV was as low as 10% of the level measured in the reference discharge, resuming quickly as the LGI action was removed, and eventually leading to the destabilization of tearing modes, at $t = 3600$ ms in 160416 and $t = 4500$ ms in 160412.

Overall, combining the reduction of carbon density and, to a lesser extent, the avoided accumulation of metal impurity, LGI pacing with small granules resulted in a reduction of the line averaged $Z_{\rm eff}$ from 2.1 to 1.8, as in the case of discharge 160414 in figure 13(*d*). On the other hand, when using larger granules, that penetrate and deposit their mass deeper in and beyond the pedestal, higher lithium concentrations are found in the core, and consequently results in values of $Z_{\rm eff}$ larger than in the reference discharge.

It is worth noticing that reduced heavy impurity accumulation was also observed with high frequency pacing with D_2 pellet pacing in DIII-D [14]. This suggest that, in the LGI pacing cases as well, the effect results from the flushing of impurities from the plasma edge by the frequent ELM crashes. On the other hand, reduced metallic impurities has been documented in ELM-free phases of lithiated H-modes in DIII-D [22], indicating that changes in the impurity transport character directly related to the presence of lithium in the plasma, as for instance reported on NSTX [24], cannot be excluded and are left to future investigation.

3.3. Divertor heat loads

Finally, in this section we focus on the characteristics of the pellet paced ELMs, with the intent of quantifying the benefits of ELM pacing in terms of reduction of heat flux.

The heat flux deposited on DIII-D divertor tiles is determined from heat conduction analysis [25] of thermography data acquired by a fast IR camera, vertically viewing the lower divertor [26, 27]. For the present experiments, the camera was run so as to acquire a radial array of pixels, at 12.0 kHz, adequate to resolve ELM dynamics. The available coverage is shown in figure 5.

Figure 14 shows the evolution of the heat flux profile measured at the outer strike point, for two selected ELM events in discharge 160409 (reference) and 160414 (LGI). The outer strike point location is visible at ≈128 cm, before the ELM. In both cases the ELM manifests itself as a sudden increase of heat flux on a wide radial region. Interestingly, in the natural ELM case, the maximal amplitude is not reached at the strike point, but ≈4–5 cm radially outwards, where a second distinct peak develops. The double peak structure is also present in the LGI-triggered ELM, but the amplitude is strongly reduced, from 500 to 200 W cm^{-2}. While secondary peaks have been documented in other experiments, for instance in JET [28], this observation differers from what was observed in former experiments of ELM pacing with deuterium pellets in DIII-D, where a single heat flux peak was measured [29]. The difference might be ascribed to the lower location of the X-point, which in the LGI discharges was closer to the divertor floor by ≈10 cm. A change of this kind is likely sufficient to reveal secondary lobes in the magnetic configuration forming in the vicinity of the x-point, during ELMs, as predicted by MHD simulations of ELM dynamics [30].

For the integrity of the plasma facing components, an important quantity is the ELM peak heat flux $q_{\rm p}$, defined as the maximum flux measured in the proximity of a divertor strike-point, over the course of an ELM event.

Figure 15 shows the radial profile of the maximum heat flux attained across the ELM duration. The two-peak structure is also visible in the ISP profile, covering a larger area due to the larger flux expansion for this equilibrium (see figure 5) at this location. A two-peak structure is also observed in ELMs induced by larger granules (0.7, 0.9 mm).

Figure 16 shows $q_{\rm p}$ computed at the inner (left) and outer (right) strike points of two discharges with ELM pacing with 0.4 mm (red markers) and 0.7 mm (cyan markers) Li granules. Each data point represents an ELM event, and is plotted as a function of the inverse of the pre-ELM period, a quantity representing the 'instantaneous' estimate of the ELM frequency. Data points from the discharge with no LGI are also included for reference. Also shown is a curve of the anticipated $q_{\rm p}$ expectation, which follows an inverse dependence on frequency, as reported in ELM pacing experiments with frozen deuterium pellet injection [5, 7, 14]. The curve is normalized

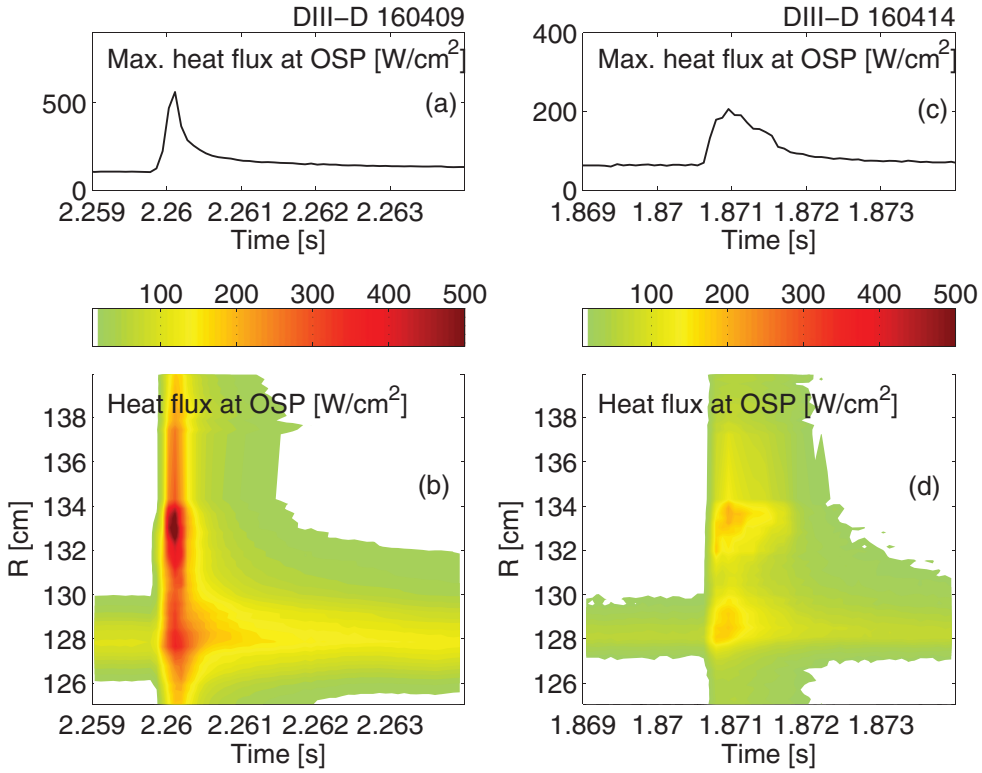

Figure 14. Evolution of the heat flux profile at the outer strike point in the case of a natural ELM (left), and a triggered ELM (right). Top panels show the maximum value attained across the profile.

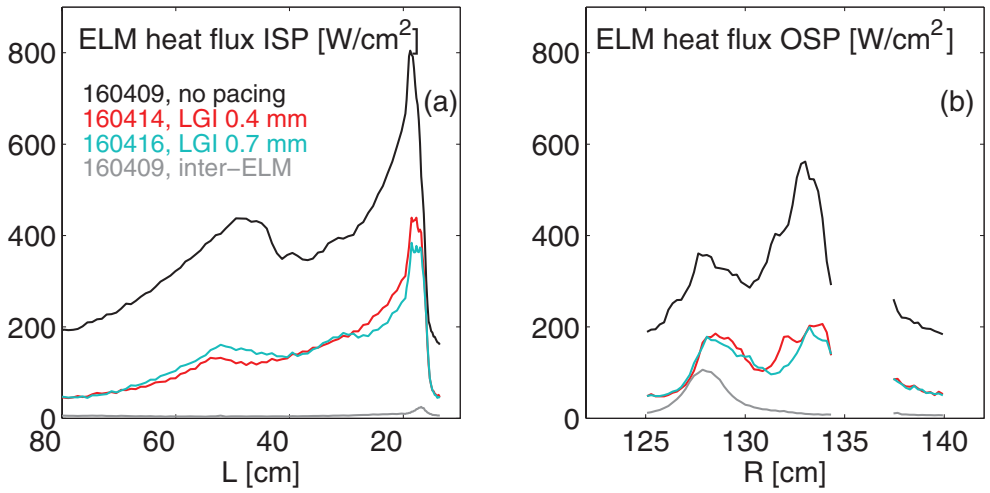

Figure 15. Profile of the maximum value of heat flux attained during a single selected ELM, in proximity to the ISP (left) and OSP (right). The ISP profile is shown as a function of the linear spatial coordinate L, which measures distances along the wall poloidal cross-sections, from the innermost point of the vessel floor.

to overlap with the data from the reference discharge. This 'statistical' representation allows for a more informative study of the results from LGI pacing experiments, which were inherently characterized by a fluctuating ELM frequency.

A noticeable spread in the measured q_p is observed, both at the inner strike point (ISP) and the outer strike point (OSP). Notice that the spread appears at constant f_{ELM}, indicating that the amplitude of the ELM event, here in terms of heat flux, does not depend strictly on the pre-ELM period. The measurements of the q_p at OSP are found in agreement with or smaller than the $1/f_{ELM}$ curve. On the other hand, the q_p at the ISP in the LGI discharges, systematically exceeded the $1/f_{ELM}$ prediction. This result, robustly reproduced in several discharges, is particularly unfavorable, given that the highest heat flux is found inboard, with $q_{p,ISP} \approx 2$–$3\ q_{p,OSP}$. These findings differ significantly from the previous experiments of ELM pacing through frozen-deuterium pellet injection (DPI) [7], where $q_{p,ISP} < q_{p,OSP}$ was reported for paced ELMs, and both quantities scaled approximately with f_{ELM}. It must be noted that, even if both experiments were performed in the same nominal scenario, the actual plasma shapes utilized were slightly different in several aspects. For instance, relative to DPI plasmas,

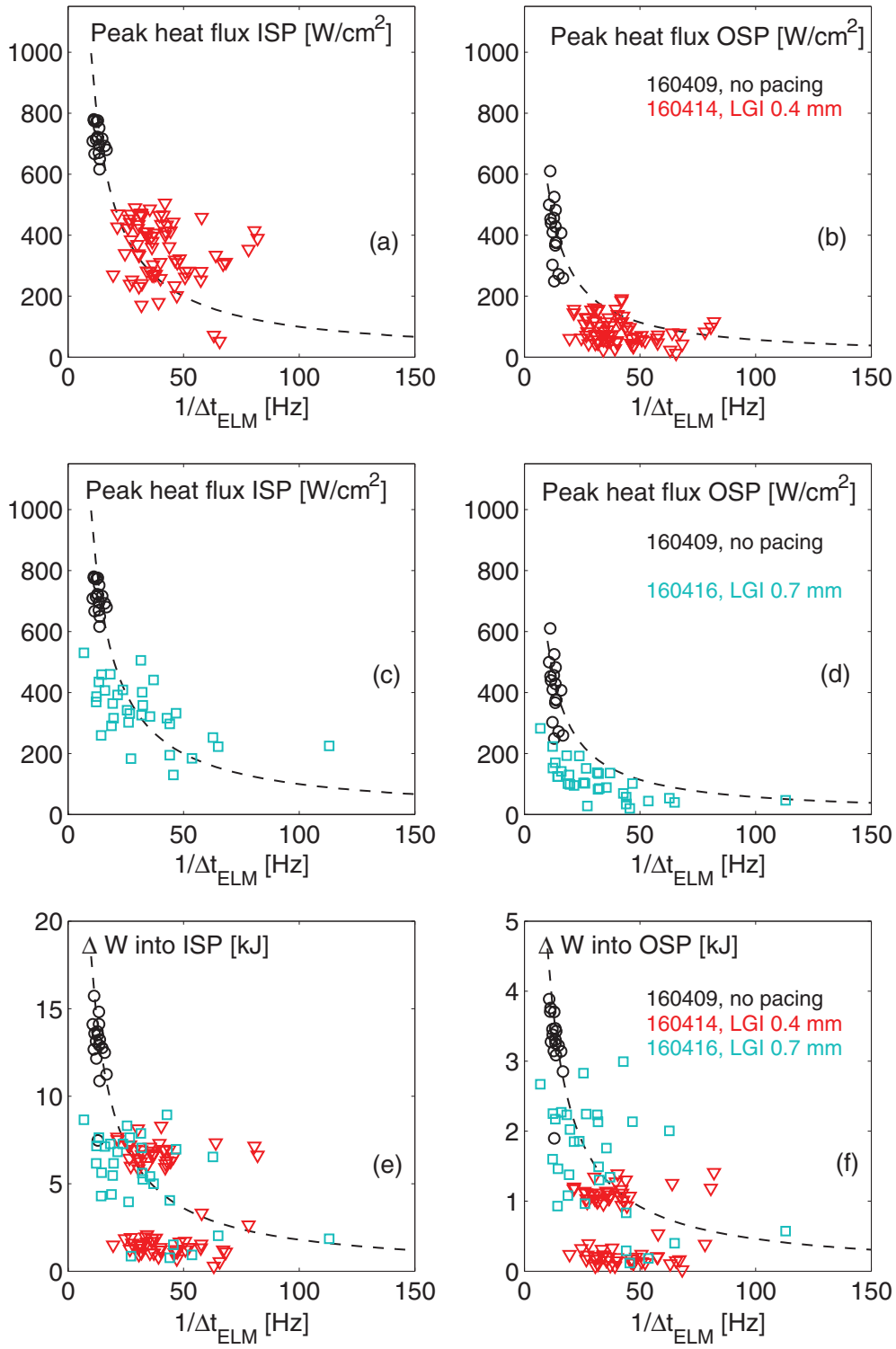

Figure 16. Statistical representation of the peak heat flux at the inner (left) and outer (right) strike points for ELM pacing with 0.4 mm ((*a*), (*b*)) and 0.7 mm granules ((*c*), (*d*)). Data are shown for each ELM event as a function of the inverse of the pre-ELM period Δt_{ELM}. The graphs include the measurements from the reference discharge without LGI pacing. ((*e*), (*f*)) Energy deposited by ELMs in the vicinity of the ISP and OSP, computed by spatial and temporal integration of the heat flux profile data.

in LGI discharges the vertical location of the divertor X-point was 10 cm closer to the vessel floor ($Z_{\mathrm{X}} = -1.10$ m), the outer gap was 5.5 cm smaller ($\Delta R = 10$ cm), and the upper triangularity was reduced by ≈40% ($\delta_{\mathrm{u}} = 0.25$).

These differences might affect significantly the SOL structure and ELM dynamics as suggested by the lower natural ELM frequency reported for the D_2 pellet pacing experiments [7].

An interesting result is found when considering the amount of energy reaching the divertor per ELM. Under the assumption of toroidal symmetry of the ELM heat deposition, this quantity is simply computed by integration of the heat flux

in space and time. The distributions of ΔW_{ISP} and ΔW_{OSP}, depicted in figures 16(*e*) and (*f*), suggest the existence of two distinct groups of ELMs characterized by ΔW which are different by a factor of 4. The distinction is also present in the q_p data, but it becomes very clear in the energy distribution, due to the shorter duration of the smaller events. Again, the fact that the two classes appear for the same range of ELM frequencies or, alternatively, pre-ELM periods, suggests that the inter-ELM evolution of kinetic profiles plays a minor role, in determining the type of ELM triggered by a granule. The inspection of the pre-ELM n_e and T_e profiles for the two classes of ELMs, determined by coherent averaging Thomson scattering measurements for a selection of ELM events, did not highlight statistically significant differences.

It is worth noticing that the smaller ELMs are not associated with sub-threshold perturbations described in section 3.1, as assured by the presence of a distinct, fast signature in the magnetics and sparse observations of natural occurrence. At this stage of the analysis, the mechanism at the origin of this separation remains under investigation.

To conclude this section, we note that the total energy deposited into the divertor per ELM from IR thermography only accounts for ≈30% of the drop in stored energy determined by fast equilibrium reconstructions. This indicates that, in this scenario, ELMs deposit a significant fraction of their energy on parts of the vessel not covered by the IR thermography, possibly including the upper divertor and the outboard first wall. This energy discrepancy might also be associated with a toroidal asymmetry of the heat flux footprint. Although toroidal asymmetries have been observed in other experiments [28], and predicted by non-linear in MHD simulations [15] of ELM triggering by pellet injection, toroidally extended thermography coverage is ultimately required to test this hypothesis.

4. Discussion

The experiments discussed in this article represent the first demonstration that in tokamak plasmas confined in H-mode, the ELM frequency can be effectively increased through injection of small lithium granules. Robust ELM pacing at increased frequency was documented for long durations, up to 3.5 s, in stationary conditions. Despite the relatively large amounts of lithium injected (up to 30 mg s^{-1}), high frequency pacing appeared to be compatible with high plasma performance, in terms of both global confinement and pedestal characteristics. This result demonstrates the possibility of using non-fuel pellet injection to pace ELMs. This may be an important option for future fusion devices with limited pumping and fuel processing throughput.

From an operational standpoint, the LGI provided extreme flexibility in choice of injection parameters, i.e. granule size, injection frequency and speed, albeit with the intrinsic limitation of a fluctuating injection frequency (see section 2). On the experimental level, this resulted in an extremely rich phenomenology, fortuitously providing unique insights into the general problem of ELM triggering and control.

Paced ELM averaged frequencies up to 100 Hz were achieved, with a 2–5 fold increase over the natural ELM frequency. Rapid sequences of injections show that inter-ELM periods smaller than 5 ms can be achieved (200 Hz), although in a transient fashion. Varying the granule velocity from 50 to 100 m s^{-1} had only a minor effect on the reliability of ELM triggering. The ELM triggering probability was found to increase with the granule mass and granules with diameter of 0.7 mm or larger appeared to be sufficient to achieve triggering efficiency >90%. The observation of 100% of ELM triggered by granules, but $f_{ELM} \ll f_{LGI}$, in discharges with 0.4 mm granules pacing, suggest a saturated maximal pacing frequency for small granule sizes. No clear evidence of an upper frequency limit has emerged when using larger granule sizes. Moreover, the transient high-efficiency, fast-paced phases obtained using 0.7–0.9 mm diameter granules suggests that high-frequency pacing at frequencies close to ITER requirements might be achievable in future dedicated experiments. However, it should be noted that, while the plasmas presented in this work were performed with a full carbon tile first-wall, recent studies of ELM pacing by deuterium pellet injection have found different efficiency and ELM characteristics when operating with carbon or high-*Z* metal walls [8, 9].

Lithium was found to penetrate deeply into the plasma volume, but there is no evidence for central accumulation, i.e. Li density peaking. Furthermore, accumulation of metallic impurities was consistently delayed or avoided by LGI pacing. Notably, in LGI paced discharges with 0.4 mm granules, peaking of T_i and T_e was observed, possibly related with lower radiative cooling or changes in energy transport or source. To discriminate between these effects a detailed characterization of the transport in LGI plasmas is required and is left for future work.

The amplitude of triggered ELMs, expressed in terms of stored energy drop ΔW, was found to vary, in a way that could not be correlated with the characteristics of the injected granules. In particular, two classes of triggered ELMs emerged, with ΔW differing by a factor of up to 4. The ELM peak heat flux at both the inner and outer strike points was observed to decrease as the ELM frequency increased. Approximate agreement with the $1/f_{ELM}$ scaling was found for q_p, at the OSP. However, a similar trend was not confirmed at the ISP, where q_p regularly exceeded the $1/f_{ELM}$ prediction. The energy deposited in the lower divertor during an ELM, inferred from IR thermography measurements, accounted for approximately 30% of the drop in stored energy. The fact that a substantial amount of energy was deposited in regions not covered by the IR thermography, might also be consistent with a toroidal asymmetry of the heat flux deposition. These results are obviously cause for concern, as they pose a challenge for the present capabilities of predicting the ELM mitigation achievable by pacing techniques. Future efforts, in experiment and modeling, are needed to clarify if these results are specific to the impurity granule pacing, or to the scenarios explored in this work, or, instead, are associated with more general aspects of the physics of ELM triggering.

MHD simulations of the non-linear destabilization of ELMs, for example with the codes JOREK [15, 31] and

M3D-C[1] [32], are planned to shed light on several intriguing aspects, for instance the variability of the ELM size obtained, the difficulty of increasing frequency over 3–5 times the natural ELM frequency using 0.4 mm granules and possible effect of background plasma rotation. To that end, a validated model for the ablation of refractory pellets, and lithium in particular, is required. The initial results reported in this work require further validation, in particular for the case of small granules, where clear discrepancies between model predictions and experimental data emerged.

Hardware upgrades are in development, which will permit better control of LGI injection frequency. The use of materials other than lithium is also actively being explored. Candidate materials for upcoming impurity granule injection experiments in DIII-D and NSTX-U are, for instance, vitreous carbon spheres, granular boron and boron carbide. These options are commercially available with degree of purity compatible with the tokamak environnement. Extending the present experiments with results with other materials would provide a unique physics base for validating ELM simulation codes and allow extrapolation to other scenarios and materials, in particular with regard to the potential use of beryllium in ITER.

Future experiments, building on the initial results presented in this initial work, will aim to demonstrate steady-state ELM pacing by impurity granules at frequencies compatible with the ITER requirements (20–50 fold increase over the natural ELM frequency).

This will provide guidance for estimating the projected amount of Be required for effective ELM mitigation in ITER, where key open issue is the formation of dust associated with the long term injection of low recycling materials.

Acknowledgments

The authors wish to acknowledge the important contribution made to this work by both the University of Illinois (U of I) and the Chinese Academy of Science Institute of Plasma Physics (ASIPP) in Hefei, China. Most of the spherical Li granules used in this work were manufactured by a process developed at U of I [33]. The manufacturing, sorting and cleaning of those granules took place at ASIPP through the combined efforts and expertise of P Fiflis (U of I) as well as Z Sun, W Xu, J Ren, X Meng and G Zuo (all of ASIPP). The authors also wish to thank J Li of ASIPP for his assistance in transferring the granules to DIII-D.

This work was supported in part by US Department of Energy (contracts DE-AC02-09CH11466, DE-AC05-00OR22725, DE-FC02-04ER54698 and DE-AC52-07NA27344).

Appendix

This section describes the method used to determine the experimental lithium density profile for the experiments included in this work, when a direct measurement was not available. The method is based on measurements from the multi-chord charge exchange diagnostic (CER), which, from the spectral analysis of the charge-exchange line CVI($n = 8 \rightarrow 7$) at 529.1 nm provides a radially and temporally resolved measurement of n_C, density of the C^{6+} ion. A byproduct of the spectral analysis is the continuum baseline of the acquired spectra, due to visible bremsstrahlung emission (VBE). By combining local measurements of n_C and chord integrated measurements of VBE, under certain conditions, the density profile of the dominant impurity can be inferred as follows.

As a first step, radially resolved measurements of electron density n_e, electron temperature T_e (e.g. from Thomson scattering), and n_C (from CER) are interpolated with smooth fit curves. An initial profile of Z_{eff} due to carbon can be constructed from $Z_{eff,C} = 1 + Z_C(Z_C + 1)n_C/n_e$ assuming that carbon is the only impurity. This is a good estimate of the actual Z_{eff} profile for cases where C^{6+} provides the dominant contribution. This is the case for plasmas without Li injection, where C^{6+} is the dominant intrinsic impurity in the plasma volume, and typically high-Z metal impurities only contribute up to 10% of Z_{eff}.

A profile of VBE emissivity at the specific wavelength of the CVI($n = 8 \rightarrow 7$) line can then be constructed, combining the n_e, T_e and $Z_{eff,C}$, and spatially integrated along the chords of CER, providing a prediction for the amplitude of the baseline emission on each CER chord. If carbon is the only species contributing to Z_{eff}, disagreement between the prediction and the actual measurements are indicative of inaccurate diagnostic calibration. In case of strong lithium injection, using $Z_{eff,C}$ leads to an underestimate of VBE. A Z_{eff} profile representative of the actual experimental quantity is found by assuming a parametric form for Z_{eff}, and adjusting the parameters so as that predictions and measurements agree. The deficit $\Delta Z_{eff} = Z_{eff} - Z_{eff,C} > 0$ is attributed to the presence of other impurities than carbon, and assuming that carbon and lithium are the only impurities, the lithium density can be obtained from $n_{Li} = \Delta Z_{eff}/Z_{Li}^2 n_e$.

An example of the results of this analysis is shown in figure A1, for discharge 160414, at $t = 3.0$ s, where agreement between VBE measurements was determined by scaling linearly the profile $Z_{eff,C}$ by a factor of 1.2.

This approach is applicable only when the concentration of other impurity species generates negligible contributions to Z_{eff}. This is especially true in the LGI-paced discharges, where the impurity content (apart from lithium) is strongly reduced.

Another caveat concerns the fact that, in DIII-D, no optical dump targets are installed to protect the CER views from, for example, reflections from in-vessel components. While this has generally a minor influence on the active part of the signal, it can affect directly the background emission. Since VBE increases quadratically with n_e, the approach just described becomes quickly less reliable for low density plasmas and close to the edge.

Notice that, the sources on inaccuracies just mentioned, if not accounted for, lead to overestimate Z_{eff}, hence the procedure describes can be used to determine an upper bound to the density of lithium.

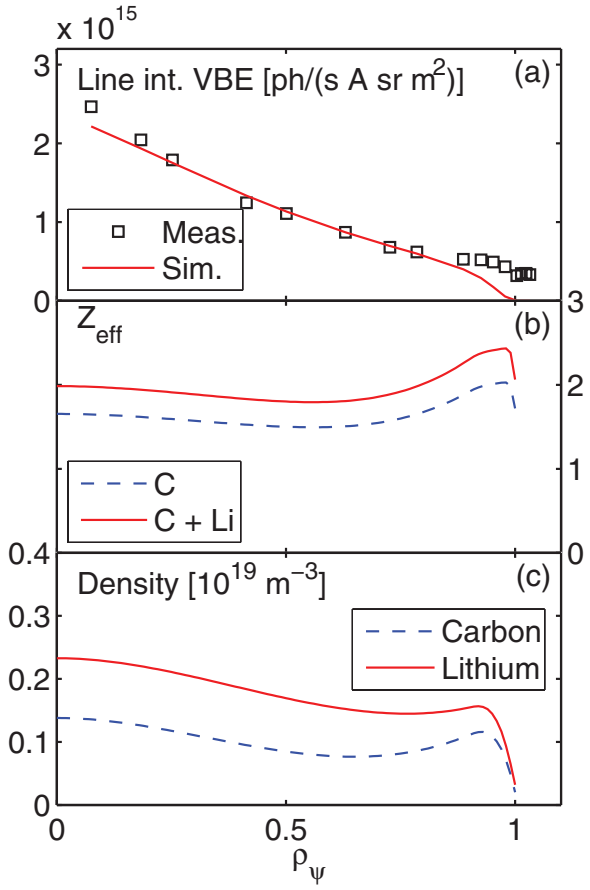

Figure A1. (*a*) Comparison between the line-integrated VBE measured by a set of tangential CER chords for a plasma discharge with LGI pacing, and the value predicted by assuming $Z_{\rm eff}$ as the red curve in (*b*). The correspondent density profiles for C^{6+} and Li^{3+} are shown in (*c*).

References

[1] Leonard A.W. 2014 Edge-localized-modes in tokamaks *Phys. Plasmas* **21** 090501

[2] ITER Physics Basis Editors *et al* 1999 *Nucl. Fusion* **39** 2137

[3] Loarte A. *et al* 2014 Progress on the application of elm control schemes to iter scenarios from the non-active phase to dt operation *Nucl. Fusion* **54** 033007

[4] Maingi R. 2014 Enhanced confinement scenarios without large edge localized modes in tokamaks: control, performance, and extrapolability issues for ITER *Nucl. Fusion* **54** 114016

[5] Lang P.T. *et al* and the ASDEX Upgrade Team 2004 Elm pace making and mitigation by pellet injection in asdex upgrade *Nucl. Fusion* **44** 665

[6] Lang P.T. *et al* and JET EFDA Contributors 2011 Elm pacing investigations at jet with the new pellet launcher *Nucl. Fusion* **51** 033010

[7] Baylor L.R. *et al* 2013 Reduction of edge-localized mode intensity using high-repetition-rate pellet injection in tokamak H-mode plasmas *Phys. Rev. Lett.* **110** 245001

[8] Lang P.T. *et al* and JET-EFDA Contributors 2013 Elm pacing and trigger investigations at jet with the new iter-like wall *Nucl. Fusion* **53** 073010

[9] Lang P.T. *et al* and the ASDEX Upgrade Team 2014 Elm pacing and high-density operation using pellet injection in the asdex upgrade all-metal-wall tokamak *Nucl. Fusion* **54** 083009

[10] Kukushkin A.S., Polevoi A.R., Pacher H.D., Pacher G.W. and Pitts R.A. 2011 Physics requirements on fuel throughput in ITER *J. Nucl. Mater.* **415** S497–500 *(Proc. of the 19th Int. Conf. on Plasma-Surface Interactions in Controlled Fusion)*

[11] Mansfield D.K. *et al* 2013 First observations of elm triggering by injected lithium granules in east *Nucl. Fusion* **53** 113023

[12] Kuninaka H. and Hayakawa H. 2004 Anomalous behavior of the coefficient of normal restitution in oblique impact *Phys. Rev. Lett.* **93** 154301

[13] Vision Research Inc. www.visionresearch.com/

[14] Baylor L.R. *et al* 2013 Reduction of edge localized mode intensity on diii-d by on-demand triggering with high frequency pellet injection and implications for iter *Phys. Plasmas* **20** 082513

[15] Futatani S., Huijsmans G., Loarte A., Baylor L.R., Commaux N., Jernigan T.C., Fenstermacher M.E., Lasnier C., Osborne T.H. and Pegouri B. 2014 Non-linear mhd modelling of elm triggering by pellet injection in DIII-D and implications for ITER *Nucl. Fusion* **54** 073008

[16] Parks P.B. and Turnbull R.J. 1978 Effect of transonic flow in the ablation cloud on the lifetime of a solid hydrogen pellet in a plasma *Phys. Fluids* **21** 1735–41

[17] Parks P.B., Gerdin G.A., Vahala L.L. and Elcashlan A.G. 1994 Model of ablation flow near light-atom pellets with surface boundary conditions *Nucl. Fusion* **34** 417

[18] Parks P.B., Leffler J.S. and Fisher R.K. 1988 Analysis of low *Z* a impurity pellet ablation for fusion diagnostic studies *Nucl. Fusion* **28** 477

[19] Lao L.L., John H. St., Stambaugh R.D., Kellman A.G. and Pfeiffer W. 1985 Reconstruction of current profile parameters and plasma shapes in tokamaks *Nucl. Fusion* **25** 1611

[20] Lore J.D. *et al* 2013 Effect of $n = 3$ perturbation field amplitudes below the elm triggering threshold on edge and sol transport in NSTX *J. Nucl. Mater.* **438** S388–92 *(Proc. of the 20th Int. Conf. on Plasma-Surface Interactions in Controlled Fusion Devices)*

[21] ITER Physics Basis Expert Groups on Confinement and Transport and Confinement Modelling and Database, ITER Physics Basis Editors 1999 *Nucl. Fusion* **39** 2175

[22] Osborne T.H. *et al* and the DIII-D Team 2015 Enhanced h-mode pedestals with lithium injection in DIII-D *Nuclear Fusion* **55** 063018

[23] Podesta M., Bell R.E., Diallo A., LeBlanc B.P., Scotti F. and the NSTX Team 2012 Measurements of core lithium concentration in a Li-conditioned tokamak with carbon walls *Nucl. Fusion* **52** 033008

[24] Scotti F. *et al* and the NSTX Team 2013 Core transport of lithium and carbon in elm-free discharges with lithium wall conditioning in NSTX *Nucl. Fusion* **53** 083001

[25] Herrmann A., Junker W., Gunther K., Bosch S., Kaufmann M., Neuhauser J., Pautasso G., Richter Th. and Schneider R. 1995 Energy flux to the ASDEX-Upgrade diverter plates determined by thermography and calorimetry *Plasma Phys. Control. Fusion* **37** 17

[26] Hill D.N., Ellis R., Ferguson W., Perkins D.E., Petrie T. and Baxi C. 1988 Infrared thermography of the DIII-D divertor targets *Rev. Sci. Instrum.* **59** 1878–80

[27] Lasnier C.J., Hill D.N., Petrie T.W., Leonard A.W., Evans T.E. and Maingi R. 1998 Survey of target plate heat flux in diverted DIII-D tokamak discharges *Nucl. Fusion* **38** 1225

[28] Wenninger R.P., Eich T.H., Huysmans G.T.A., Lang P.T., Devaux S., Jachmich S., Köchl F. and JET EFDA Contributors 2011 Scrape-off layer heat transport and divertor power deposition of pellet-induced edge localized modes *Plasma Phys. Control. Fusion* **53** 105002

[29] Baylor L.R. *et al* 2015 Elm mitigation with pellet ELM triggering and implications for pfcs and plasma performance in ITER *J. Nucl. Mater.* **463** 104–8 *(Proc. of the 21st Int. Conf. on Plasma-Surface Interactions in Controlled Fusion Devices (Kanazawa, Japan, 26–30 May 2014))*

[30] Huijsmans G.T.A. and Loarte A. 2012 *Proc. 24th Int. Conf. on Fusion Energy (San Diego, 2012)*, ITR/P1-23 (http://www-naweb.iaea.org/napc/physics/FEC/FEC2012/papers/164_ITRP123.pdf)

[31] Huysmans G.T.A., Pamela S., van der Plas E. and Ramet P. 2009 Non-linear mhd simulations of edge localized modes (elms) *Plasma Phys. Control. Fusion* **51** 124012

[32] Ferraro N.M. and Jardin S.C. 2009 Calculations of two-fluid magnetohydrodynamic axisymmetric steady-states *J. Comput. Phys.* **228** 7742–70

[33] Fiflis P., Andrucyzk D., Roquemore A.L., McGuire M., Curreli D. and Ruzic D.N. 2013 Lithium pellet production (LIPP): a device for the production of small spheres of lithium *Rev. Sci. Instrum.* **84** 063506